

This is a repository copy of An application of a MEMS vector hydrophone for condition assessment of a water supply pipe.

White Rose Research Online URL for this paper: https://eprints.whiterose.ac.uk/id/eprint/232836/

Version: Published Version

Article:

Shi, P., Yu, Y., Watts, J. et al. (2 more authors) (2025) An application of a MEMS vector hydrophone for condition assessment of a water supply pipe. Applied Acoustics, 231. 110449. ISSN: 0003-682X

https://doi.org/10.1016/j.apacoust.2024.110449

Reuse

This article is distributed under the terms of the Creative Commons Attribution (CC BY) licence. This licence allows you to distribute, remix, tweak, and build upon the work, even commercially, as long as you credit the authors for the original work. More information and the full terms of the licence here: https://creativecommons.org/licenses/

Takedown

If you consider content in White Rose Research Online to be in breach of UK law, please notify us by emailing eprints@whiterose.ac.uk including the URL of the record and the reason for the withdrawal request.



ELSEVIER

Contents lists available at ScienceDirect

Applied Acoustics

journal homepage: www.elsevier.com/locate/apacoust





An application of a MEMS vector hydrophone for condition assessment of a water supply pipe

Pengcheng Shi ^a, Yicheng Yu ^{b,*}, Joanna Watts ^b, Guojun Zhang ^a, Kirill V. Horoshenkov ^b

- a State Key Laboratory of Dynamic Measurement Technology, North University of China, Taiyuan, China
- ^b Department of Mechanical Engineering, University of Sheffield, Mappin Street, Sheffield, UK

ARTICLE INFO

Keywords:
Pipe inspection
MEMS
Vector hydrophone
Particle velocity
Leakage

ABSTRACT

This paper describes an application of a micro-electromechanical system (MEMS) vector hydrophone to detect 10–20 mm wall damage in a 300 mm diameter ductile iron pipe used for water distribution. A key novelty of this work is the use of the acoustic pressure and particle velocity measured in the vicinity of the pipe wall at frequencies of sound with wavelengths much greater than the pipe diameter, i.e. below 400 Hz. It is shown through numerical simulation and laboratory experiment that the acoustic particle velocity, unlike the acoustic pressure, is highly sensitive to the presence of relatively small wall damage. This work paves the way for the development of new sensor solutions that can be deployed on inspection robots in pressurized clean and wastewater pipes to localize the onset of wall damage. Machine learning algorithms could be used to train the robot to recognize signal patterns associated with an in-pipe defect to guide maintenance and repair equipment.

1. Introduction

In the UK there over 300,000 km of buried pipes that supply clean water. In addition, there are over 30,000 km of pressurized rising mains that pump sewage up a gradient to water treatment plants [1,2]. A large proportion of these pipes are made of cast iron or ductile iron that deteriorate gradually leading to bursts which can cause considerable water loss, road closures and pollution [3,4]. Additionally, even a minor leakage from these deteriorating pipes can have negative consequences, highlighting the overall impact of their degradation [5,6]. The causes of pipe wall deterioration are hard to predict therefore it is important to carry out preventative inspection and maintenance to stop bursts from happening [7–9]. Currently this is difficult and expensive because there is uncertainty and risk regarding which sections need surveying, in addition to which mains are often hard to access and logistically difficult to shut off [10,11].

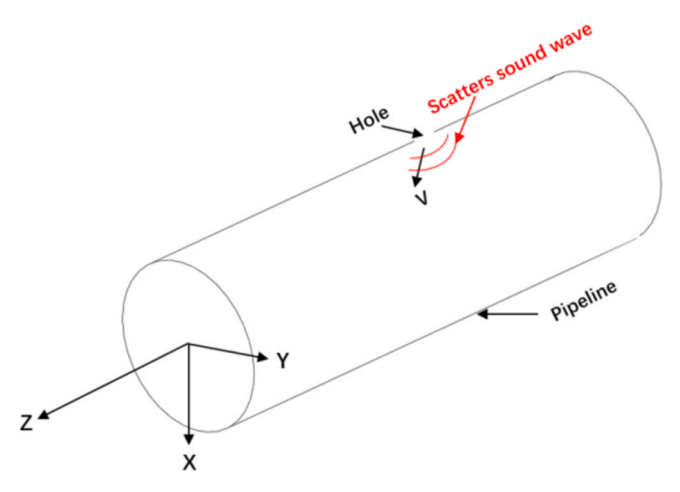
A very common technique to detect damage and wall loss in iron pipes has been to use non-destructive evaluation (NDE) methods. These methods are typically based on the magnetic, electrical and ultrasonic properties of the pipe wall material. A good review of these methods can be found in [12,13]. Such methods rely on the detection of some level of change in the properties associated with the presence of an unexpected secondary phase, such as the degradation due to the presence of

corrosion or cracking. The use of these methods in the field is problematic and many of them are limited to the laboratory. Key issues are the inherent variation in the microstructure of iron, its graphite flake structure, poor surface condition, e.g. the transition zone of active corrosion [14–16]. These factors significantly attenuate ultrasonic signals and distort electromagnetic signals, making their interpretation difficult [17,18]. Additionally, these inspection methods are slow, requiring complex sensor arrays, signal processing methods, and fast processing power [13].

Due to the excellent vector and directional properties of MEMS vector hydrophones, they have been widely applied in detecting weak distant noises from submarines and underwater target detection [19,20]. The vector hydrophone consists of cantilever beams and ciliary structures that mimic the lateral line organs of fish. By sensing sound waves through the cilia, it can effectively detect underwater acoustic signals. Therefore, this paper is the first to apply the MEMS vector hydrophone to pipeline detection and proposes a pipeline leak detection method based on MEMS vector hydrophones to detect acoustic signals in the pipeline [21,22]. The sensors can simultaneously measure the acoustic pressure and three components of the acoustic particle velocity vector near the pipe wall. It is shown that the acoustic particle velocity, unlike acoustic pressure, is very sensitive to the onset of small damage in a ductile iron pipe. It is also shown that the acoustic vector hydrophone

E-mail address: Yicheng.Yu@sheffield.ac.uk (Y. Yu).

^{*} Corresponding author.



 ${\bf Fig.~1.}$ An illustration of the problem of sound propagation in a pipe with a defect.

is very effective at frequencies of sound at which the acoustic wavelength is much greater than the pipe diameter. Despite their long wavelength, some characteristics of these waves are highly sensitive to

-0.1

y [m]

0

0.1

Table 1
Pipe parameters used in the models.

Parameter	Value	Units
pipe radius	0.15	m
pipe wall thickness	0.01	m
pipe length (L_p)	56	m
Distance from source to defect (d_s)	1	m
for cutout: minimum wall thickness	0.003	m
for cutout: radius of cutout	0.143	m
for cutout: maximum size of mesh next to cutout	0.003	m
for hole: radius	0.015	m
for hole: maximum size of mesh next to hole	0.005	m
PML length (L_{PML})	1	m
segments in PML	8	
length of 3D meshed region (L_{3D})	0.21	m
maximum element size	0.05	m
Young's modules, ductile iron	172	GPa
Poisson ratio, ductile iron	0.275	
density, ductile iron	7150	kg/m ³
bulk modulus of water	2.2 GPa	
density, water	1000	kg/m ³

0.1

z [m]

-0.1

y [m]

0

0.1

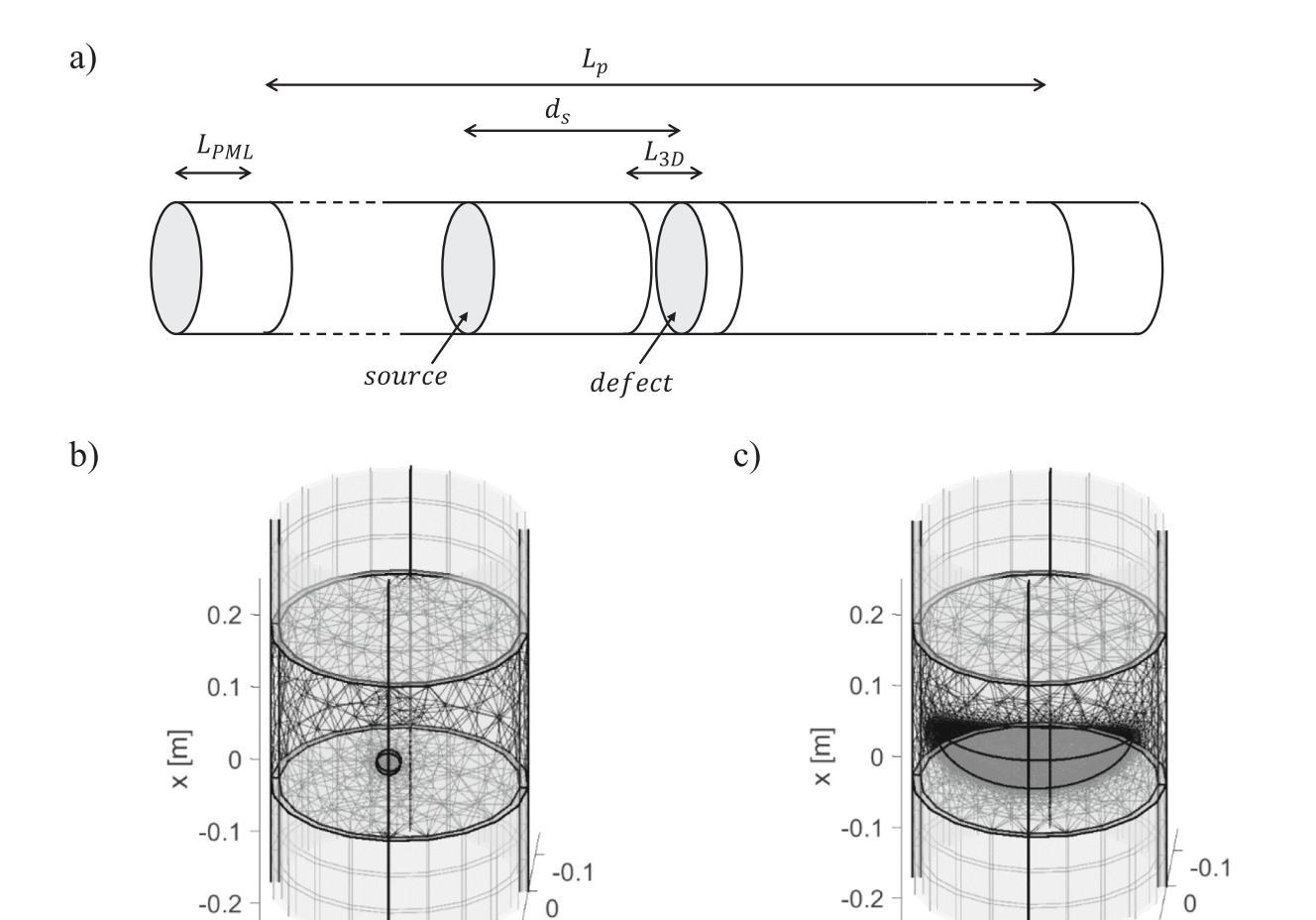


Fig. 2. Comsol models. (a) schematic view of the model showing the main components: perfectly matched layers (PMLs) at each end, a planar source located d_s from the plane at the center of the defect, and a region with length L_{3D} centered on the defect which uses a 3D tetrahedral mesh rather than the swept mesh used elsewhere. The entire body of the pipe has length L_p . (b) A view of the model of a 30 mm diameter hole in the side of the pipe, showing the mesh. (c) A view of the model representing thinning of the pipe wall where a sphere has been cut away from the pipe wall such that the pipe wall is reduced to 1/3 of its initial thickness at the maximum depth and the transition to this degree of thinning is smooth. Again, the mesh around the region of interest is shown.

z [m]

0.1

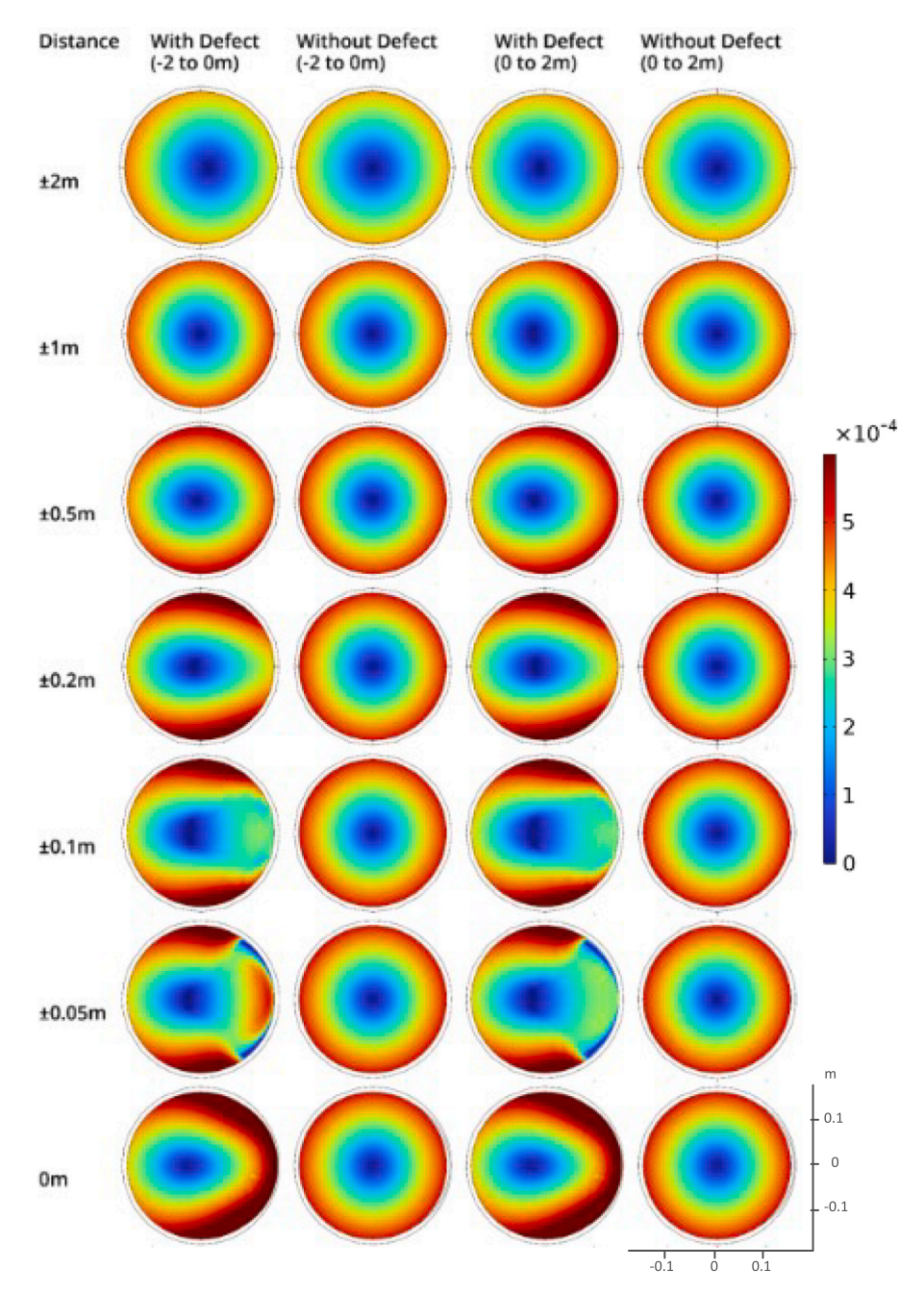


Fig. 3. Results of the radial particle velocity with and without a defect for distances between -2 m and +2 m from the defect, here the defect is a thinning of the pipe wall on the right-hand side of the pipe. The pipe has been excited with a 65 Hz plane wave 1 m from the defect. The color scale is 0-0.6 mm/s.

wall damage. These sound waves are generated in water distribution pipes by pumps or inherently present due to background noise so that these are naturally available to support wall damage detection. These waves are also relatively easy to excite artificially if required through hydrants or air vents. Low frequency, long wavelength waves propagate very long distances at a relatively low attenuation and so are viable to be used for damage detection by robots equipped with acoustic vector hydrophones as shown in this paper.

2. Theory and methods

2.1. Acoustic waves in a pressurized water pipe

Fig. 1 illustrates the problem of sound propagation in a pipe with scattering from a defect. If the frequency of sound is below the ring

frequency, f_r , of the pipe [23,24]:

$$f_r = \frac{c_i}{2\pi R} \tag{1}$$

i.e. $f \ll f_r$, then the fluid-borne wave in the pipe is close to being planar. f_r in Eq. (1) is the ring frequency at the which the wavelength of a longitudinal wave in the pipe material equals its circumference, c_i is the sound speed of the pipe material, R is the radius of the pipe.

This means that the acoustic pressure in the plane wave does not depend on the radial and angular sensor position in the pipe and can be expressed as a function of the axial coordinate z and time t as:

$$p(t,z) = p_0 e^{j(\omega t - kz)}$$
 (2)

where ω is the angular frequency of the acoustic signal, $j = \sqrt{-1}$, and

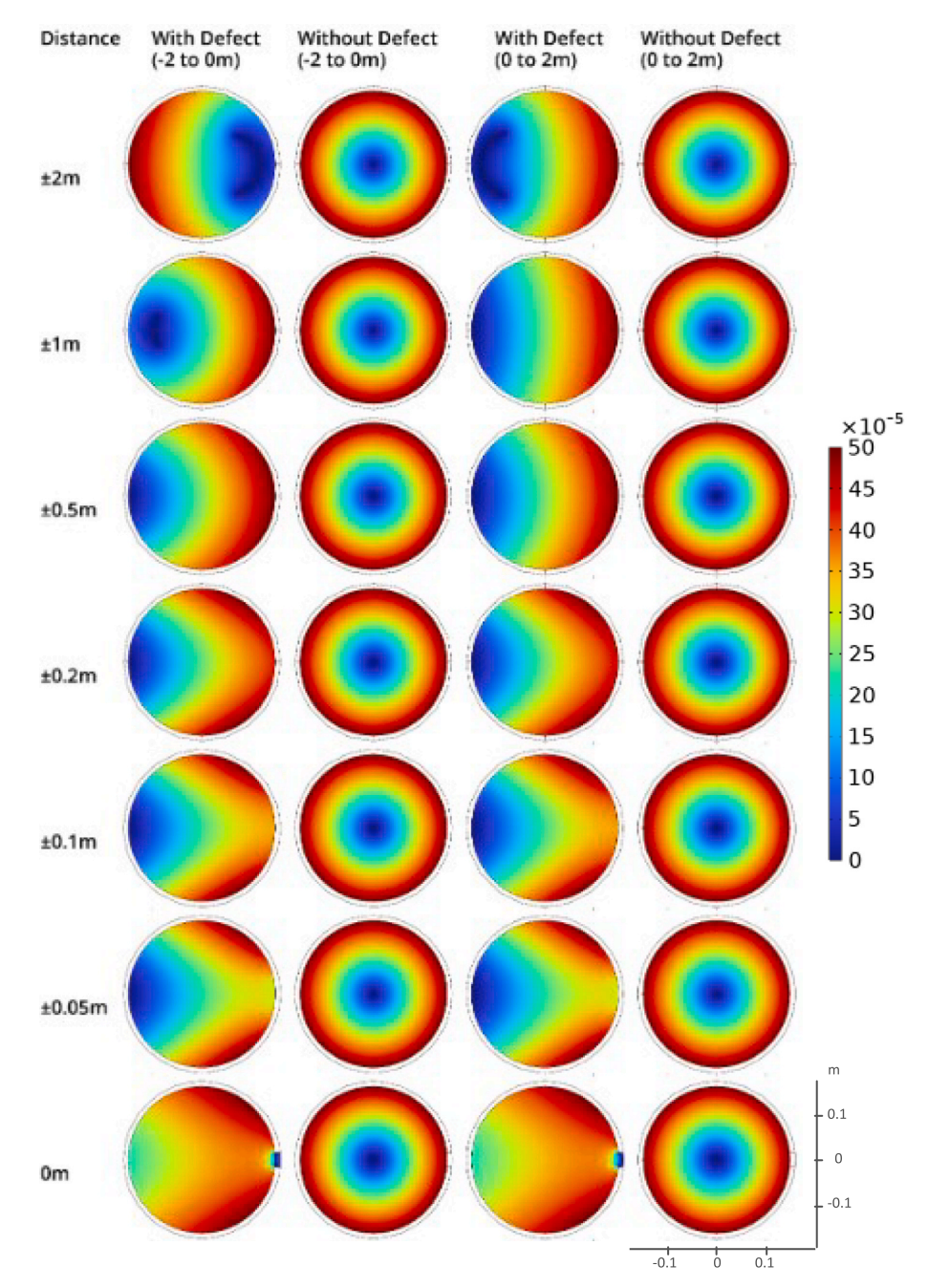


Fig. 4. Results of the radial particle velocity with and without a defect for distances between -2 m and +2 m from the defect. Here the defect is a hole in the pipe wall on the right-hand side of the pipe. The pipe has been excited with a 65 Hz plane wave excited by a point source at 1 m from the defect. The color scale is 0-0.5 mm/s.

 $k=\omega/c$ is the acoustic wavenumber. In this situation the acoustic wave propagation velocity can be described as [25,26]:

$$c = c_f / \sqrt{1 + \frac{2B_f}{\frac{E_i h_i}{R} - \omega^2 \rho_i R h_i + 2G_m}}$$
(3)

In the above equation c_f and B_f are the free field sound speed in and bulk modulus of water, E_i and ρ_i are the Young's modulus and density of pipe wall, h_i is the pipe wall thickness and G_m is the shear modulus of the soil surrounding the pipe. Eq. (3) suggests that the sound speed in the fluid in a typical ductile iron pipe is only 10–20 % slower than $c_f\cong 1500$ m/s or over 1500 times faster than the usual flow velocity of 1 m/s.

Any wall damage scatters the plane wave so that the total acoustic pressure in the vicinity of this damage becomes:

$$p_d(x, y, z, t) = p(z, t) + p_s(x, y, z, t),$$
(4)

where $p_s(x,y,z,t)$ is the acoustic pressure scattered by the defect, p_d is the total acoustic pressure, p is the incident sound pressure. Because $|p_d| \approx |p|$ and $|p_s| \ll |p|$ at low frequencies, it is problematic to detect the presence of damage by measuring the acoustic pressure in the pipe. This intrigues the concept of using particle velocity for defects detection. It can be noted that $\frac{\partial p_d}{\partial x}, \frac{\partial p_d}{\partial y} \neq 0$ near the defect whereas $\frac{\partial p}{\partial x}, \frac{\partial p}{\partial y} \approx 0$ everywhere in the pipe, because the propagating wave is planar as defined by Eq. (1). The acoustic velocity vector $\overline{u} = (u_x, u_y, u_z)$ is defined as [25]:

$$\overline{u} = \frac{\overline{\nabla}p}{\mathrm{i}\omega\rho_o},\tag{5}$$

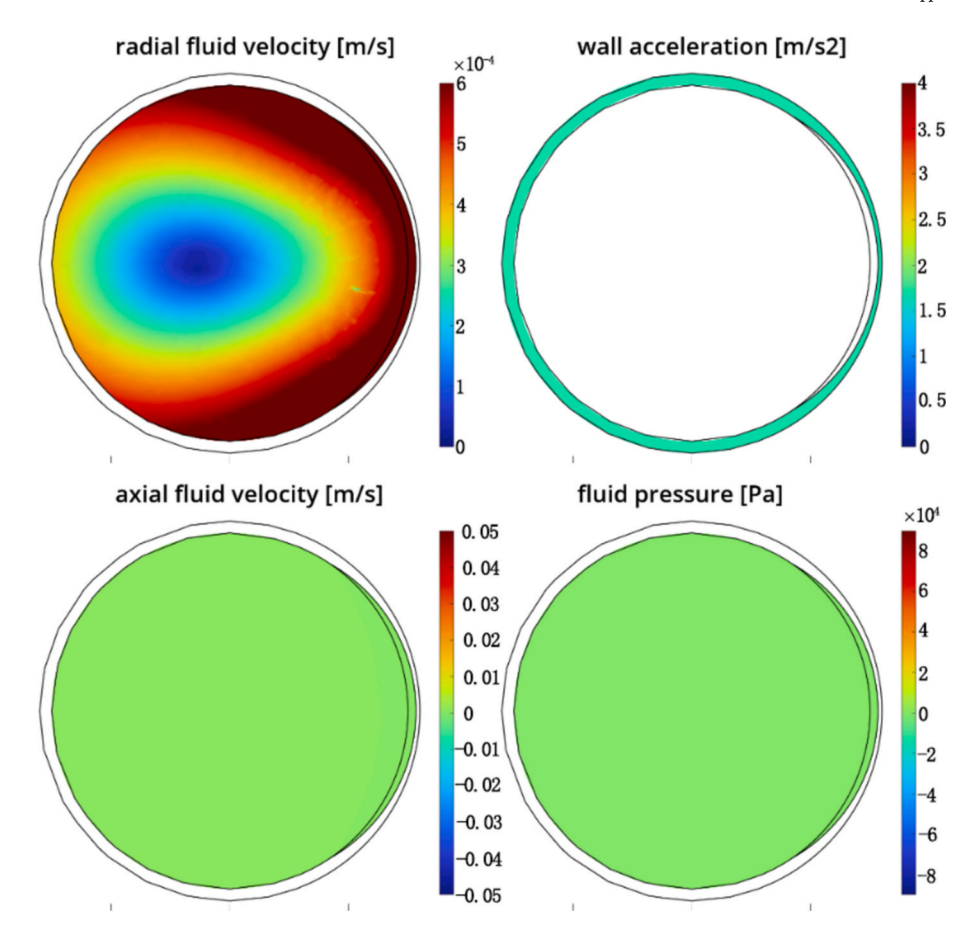


Fig. 5. A comparison of acoustic properties at the defect location. The scales have been chosen to reflect the variation in each variable along the length of the pipe.

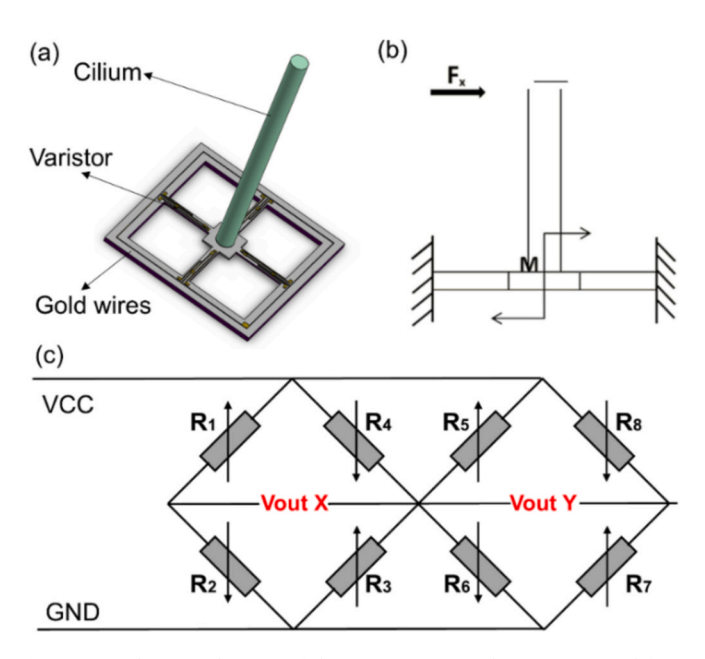


Fig. 6. (a) Schematic diagram of the microstructure; (b) cross-sectional force diagram of the microstructure; (c) schematic diagram of the Wheatstone bridge circuit.

i.e. it is proportional to the acoustic pressure derivative. In the above equation, ρ_0 is the water density. The u_x , u_y components of the acoustic (particle) velocity vector corresponding to the total acoustic pressure p_d near the defect are small in comparison with the u_z component but

measurable with a sensitive enough vector hydrophone (also called an intensity probe) as discussed in the following sections.

When the sensor is located close to the scatter, where both the propagating (planar wave below the ringing frequency) and evanescent wave can be captured, the scattered wave $p_s(r,t)$ can be expressed using Kirchhoff–Helmholtz integral or Rayleigh integral as:

$$p_{s}(\mathbf{r},t) = \iint_{dA} \left[G(\mathbf{r}|\mathbf{r}',t) \frac{\partial}{\partial \mathbf{r}} p_{d}(\mathbf{r}',t) \right] d\mathbf{r}'$$
 (6)

where dA is the integration area around the pipe defects, $\mathbf{r}=(x,y,z)$ which is the coordinate of the receiving point, $\mathbf{r}'=(x',y',z')$ is the position at the source or the pipe defects and \mathbf{n} is the normal to the pipe wall. $G(\mathbf{r}|\mathbf{r}',t)$ is the Green's function which can be expressed with modal superposition [26]:

$$G(\mathbf{r}|\mathbf{r}',t) = \frac{j}{2\pi} \sum_{m,n} \frac{J_m(k_{mn}r)J_m(k_{mn}r')}{Q_{mn}J_m(k_{mn})^2} e^{j[\omega t - \sqrt{k^2 - k_{mn}^2}|z - z'|]}$$
(7)

where Q_{mn} is pipe wall impedance, $r=\sqrt{x^2+y^2}$, $r'=\sqrt{x'^2+y'^2}$, k_{mn} is the radial wavenumber normalized by the pipe radius, R. Specifically, when m=n=0, G(r|r',t) reduces to the plane wave mode, resulting in zero $\nabla_x G$, $\nabla_y G$ derivatives. Whereas when $m\neq 0$, or $n\neq 0$, the derivatives of the Green's function with respect to x or y, $\nabla_x G$, $\nabla_y G$, are not zero. The elevated modal components contribute to the discernible (measurable) u_x, u_y elements of the acoustic velocity vector, which are associated with the total acoustic pressure in proximity to the defect. It is important to acknowledge that these higher modal components exhibit evanescent characteristics below the ringing frequency, characterized by a rapid decay along the pipe's axial direction. Consequently, the scattering effects induced by a defect are predominantly sensitive within

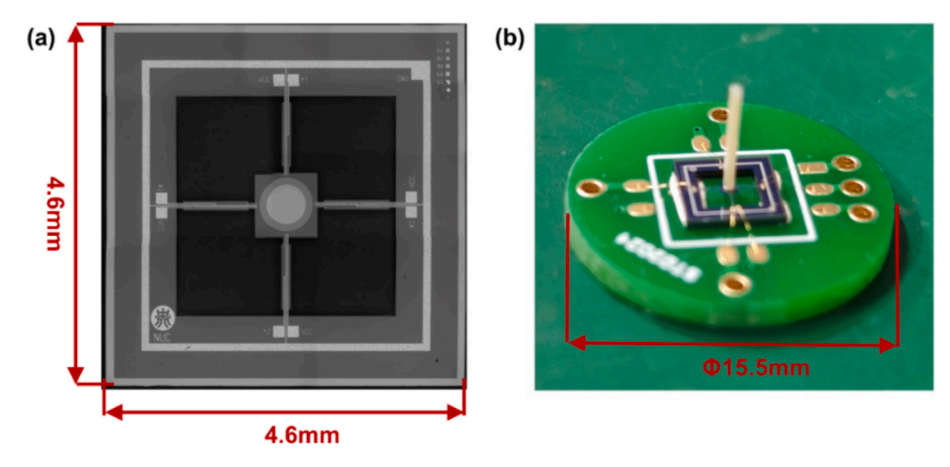


Fig. 7. (a) crossbeam microstructure of the MEMS vector hydrophone under the microscope, (b) MEMS vector hydrophone microstructure.

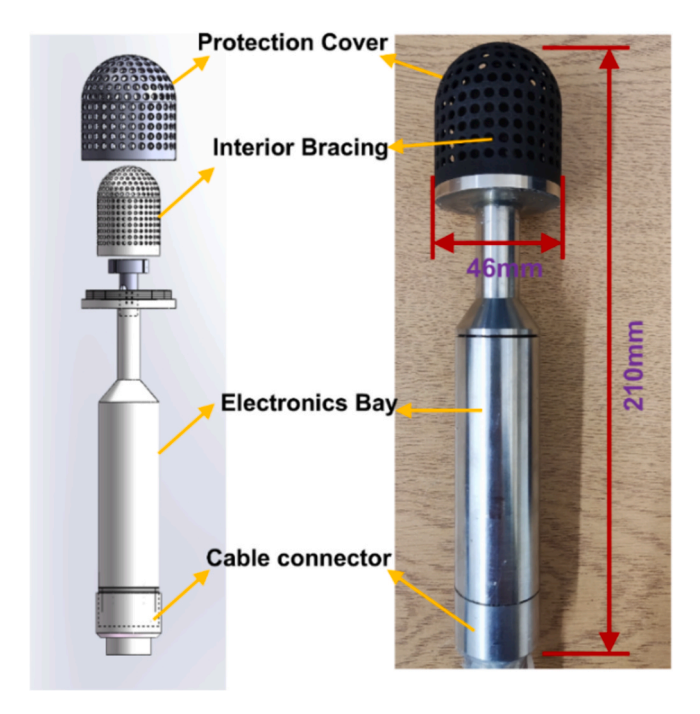


Fig. 8. A photograph of the MEMS Vector Hydrophone.

the nearfield region, facilitating precise localization of the defect.

2.2. Numerical simulation

The use of low frequency acoustic waves (where the wavelength of sound is much greater than the pipe diameter) to detect wall thickness losses is attractive because these waves can propagate considerable distance with little attenuation and are relatively unaffected by the presence of gas or impurities in the fluid. In many cases, low frequency sounds in a pressurized water pipe are generated by pumps, valves or leaks, and these could be used as a naturally present acoustic stimulus, removing the need to introduce the sound to the pipe and the ensuant practicalities. The effect of a loss of wall thickness on low frequency acoustic pressure waves in a fluid-filled pipe is relatively small such that it is difficult or impossible to measure with traditional sensors such as hydrophones or other types of pressure transducer. However, this section of the report is focused on modelling the propagation of low frequency acoustic waves in the presence of a defect to illustrate that acoustic velocity sensors can be used to detect the onset of wall damage.

The numerical simulations presented in this paper were focused on

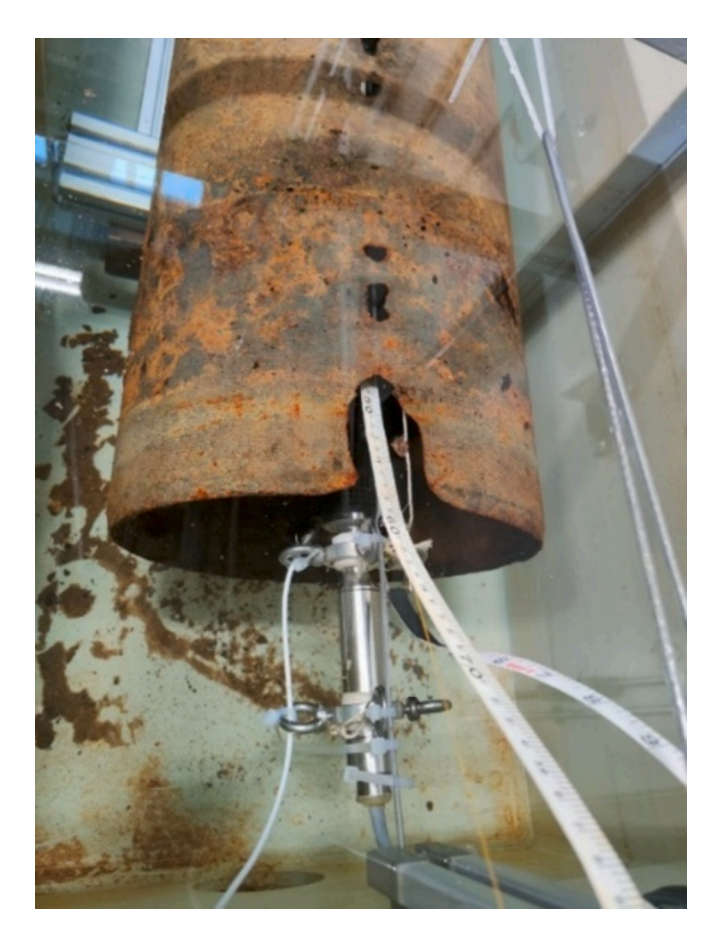


Fig. 9. A photograph of the pipe setup with the vector hydrophone inserted in the pipe at one end and speaker at the opposite end.

the problem of detecting small holes in the pipe wall, and it was assumed that in many cases this would start as a thinning of the pipe wall, which subsequently broke through to form a hole. As such two simulations were run, one looking at a hole in the pipe wall and the other investigating the effect of localized thinning of the pipe wall. The effect of these defects on the acoustic pressure and velocity were all modelled in COMSOL Multiphysics $^{\text{TM}}$ for a ductile iron pipe with a 300 mm internal diameter and 10 mm thick wall, as shown in Fig. 2. The geometrical and material parameters used in the model are provided in Table 1. The hole in the wall (Fig. 2(b)) and thinning of the pipe wall (Fig. 2(c)) were simulated by replacing the local cast iron material properties at the mesh

Fig. 10. Schematic diagram of the leak hole testing in the water pipeline.



Fig. 11. Distribution of leak holes on the water pipe.

nodes with the values that corresponded to water. From these models the behavior of the acoustic velocity vector \overline{u} was predicted, analyzed and compared against that of the total acoustic pressure p_d .

The results for the radial particle velocity are shown in Figs. 3 and 4 for the internal thinning defect and the hole defect, respectively. Each of the two figures shows the results of the simulation at a range of distances for the cases with and without the defect. The results for the case without the defect are included to demonstrate that the change was due to the properties of the simulation beyond the change to the mesh. In this case the defected area was filled in with the pipe material rather than fluid to conceal it from the model.

When the pipe wall is continuous and does not contain any defects, the absolute value of the radial component of the acoustic velocity is symmetric across the pipe cross-section and constant along the pipe length. In contrast, in the presence of a defect this symmetry is broken and the velocity varies with distance from the defect. This is a significant, detectable change. The same behavior is not seen for other acoustic quantities of interest, e.g. acoustic pressure, axial velocity and wall

acceleration. Fig. 5 shows the results for a pitting defect where it can be seen that there is very little variation in the axial velocity, acoustic pressure or wall acceleration.

These models have demonstrated that when the thickness of the pipe wall reduces locally, because of corrosion, graphitization or other structural damage, the amplitude of the radial component increases and varies significantly across the pipe as illustrated in Figs. 3 and 4 for distances to the defect of 0.05 m or less. At these distances the behavior of the u_x and u_y component of the acoustic velocity becomes complex and its absolute value is detectable. There is a clear difference between the behavior of the radial component of the acoustic velocity for the nodefect case, local internal pitting, local external pitting and overall thinning in the pipe diameter.

3. MEMS vector hydrophone

To measure the particle velocity components, a specialized vector hydrophone is required. A comprehensive examination of hydrophone

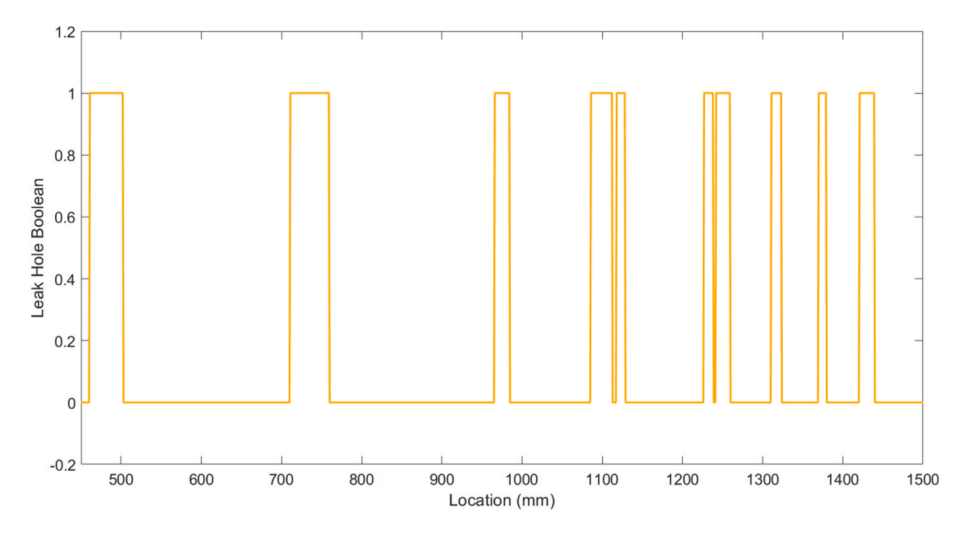


Fig. 12. Statistical chart of the positions and aperture sizes of leakage holes in the water pipe.

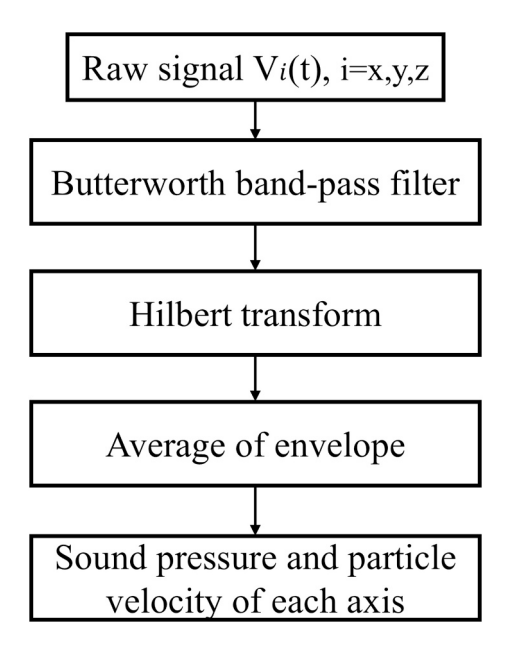


Fig. 13. Flowchart of data analysis process.

technology, encompassing vector hydrophones, is provided in Refs. [21,22]. The microstructure of the MEMS vector hydrophone used in this work consists of cilia-crossbeam. The schematic diagram of the microstructure is shown in Fig. 6 (a). Underwater acoustic waves propagated through the acoustic hood of the sensor are sensed by the cilia installed in the middle. The cilia oscillate when exposed to the underwater acoustic wave that cause the deformation in the cantilever beam. The force on the microstructure interface of the MEMS vector hydrophone is illustrated in Fig. 6 (b). The Wheatstone bridge principle on the crossbeam of the MEMS vector hydrophone is depicted in Fig. 6 (c). The piezoresistive resistor on the cantilever beam forms the Wheatstone bridge, which converts the resistance change caused by the deformation of the cantilever beam into a corresponding change in output voltage, thereby achieving the conversion from acoustic signals to electrical signals.

Four piezo-resistors with equal resistance values are implanted on the cantilever beam to form a Wheatstone bridge (see Fig. 6). Under the application of a DC voltage, the cantilever beam undergoes deformation, and the output differential voltage is [27]:

$$V_{\text{out}} = \frac{(R_1 + \Delta R_1)(R_3 + \Delta R_3) - (R_2 - \Delta R_2)(R_4 - \Delta R_4)}{(R_1 + \Delta R_1 + R_2 - \Delta R_2)(R_3 + \Delta R_3 + R_4 - \Delta R_4)} V_{CC}$$
(8)

 V_{out} is the output voltage of the bridge, V_{CC} is the power supply voltage, and ΔR is the resistance change.

The picture of the crossbeam microstructure of the MEMS vector hydrophone under the microscope is shown in Fig. 7 (a). The physical diagram of the MEMS vector hydrophone microstructure is shown in Fig. 7 (b). The vector hydrophone contains two Wheatstone bridges, so it can achieve vector measurement of acoustic signals.

The left side of Fig. 8 is a structural diagram of the overall package of the MEMS vector hydrophone, and the right side of Fig. 8 shows a photograph of the MEMS vector hydrophone assembly. The assembly of the MEMS vector hydrophone includes the cilia-crossbeam sensitive structure, protective casing, support net, electronic compartment, and cable connectors. In comparison to acoustic pressure hydrophones, the MEMS vector hydrophone used in this work can simultaneously measure the u_x and u_y acoustic velocity in addition to the acoustic pressure p_d . Therefore, it has a significant advantage in detecting wall defects in water pipelines because of the reasons presented in the previous section.

4. Pipeline leakage testing

4.1. Pipeline experimental setup

An exhumed 2.5 m long section of a 300 mm ductile iron pipe was used in the experiment reported in this section. The pipe wall thickness was 10 mm. The pipe was fully submerged in water in a container as shown in Fig. 9. The pipe had the underwater speaker (Visaton FR 8 WP) fixed at one end and the sensor inserted at the other end. A calibrated Bruel & Kjaer Type 8103 hydrophone was attached to the MEMS vector hydrophone to measure the acoustic pressure. In the reported experiment the MEMS vector hydrophone was used to measure the u_x and u_y velocity components only. The speaker was fixed in the middle of the pipe's cross-section. Considering the sensor's protective cover width of 46 mm and the need to reduce boundary effect interference, the sensor was inserted so that its center was 100 mm from the top wall of the pipe. The sensor was moved with a string attached to a system of pulleys. At each sensor position the speaker emitted a 5 sec long 65 Hz sine wave signal in the pipe.

The sensor was initially inserted at $z_s = 450$ mm from the pipe end. It was then moved in 50 mm steps to 1500 mm into the pipe. The detected voltage signals from the two hydrophones were recorded at a sampling rate of 10 kHz using a data acquisition module (NI USB-4431). A photograph of the setup is provided in Fig. 9 and the experiment is

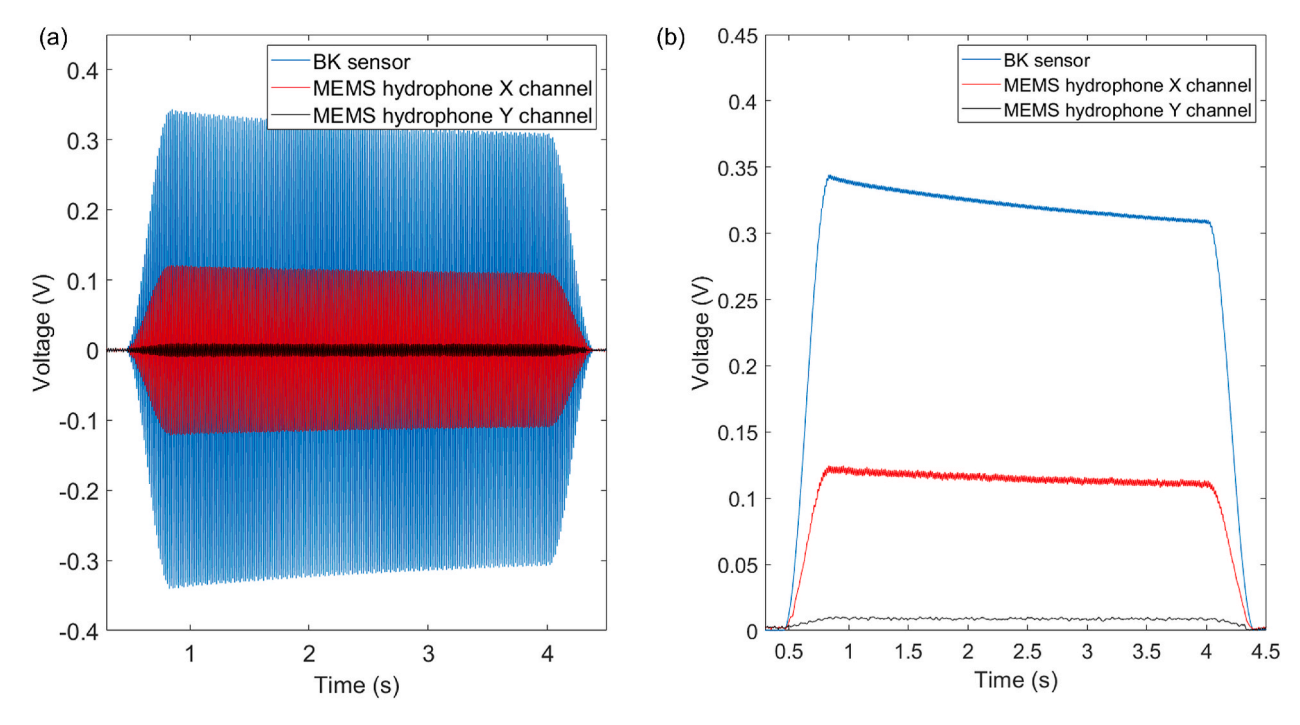


Fig. 14. (a) Raw voltage signals received by BK hydrophone and MEMS hydrophone at 600 mm. (b) Extracted Hilbert envelope of the signals.

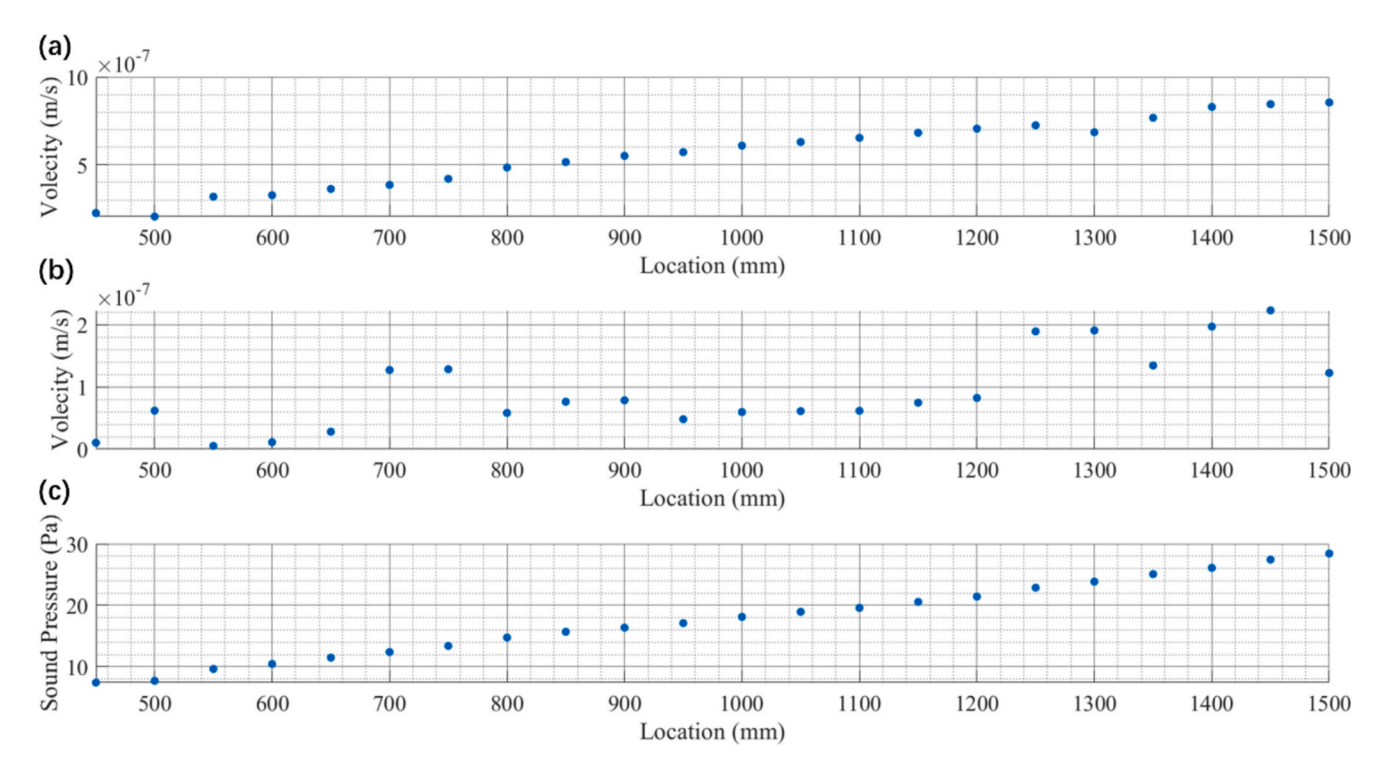


Fig. 15. (a) the time average velocity amplitude along the *x*-axis, (b) the time average velocity amplitude along the *y*-axis, and (c) the time average amplitude of the sound pressure as a function of the sensor location for the 65 Hz sine excitation.

explained schematically in Fig. 10. The distribution of leakage holes on the water pipeline is shown in Fig. 11. Fig. 12 is a chart depicting the positions and sizes of the leakage holes on the water pipeline. Positions with leakage holes are represented by 1, while positions without leakage holes are represented by 0.

4.2. Data analysis

Fig. 13 illustrates the data analysis process applied to the collected signals. The voltage signals collected by the sensor at 65 Hz were filtered using third-order Butterworth bandpass filters with the corresponding center frequencies and a bandwidth window of 40 Hz. The selected filter order was checked to ensure that it provided a numerically stable output signal with a flat amplitude response between the cutoff frequencies.

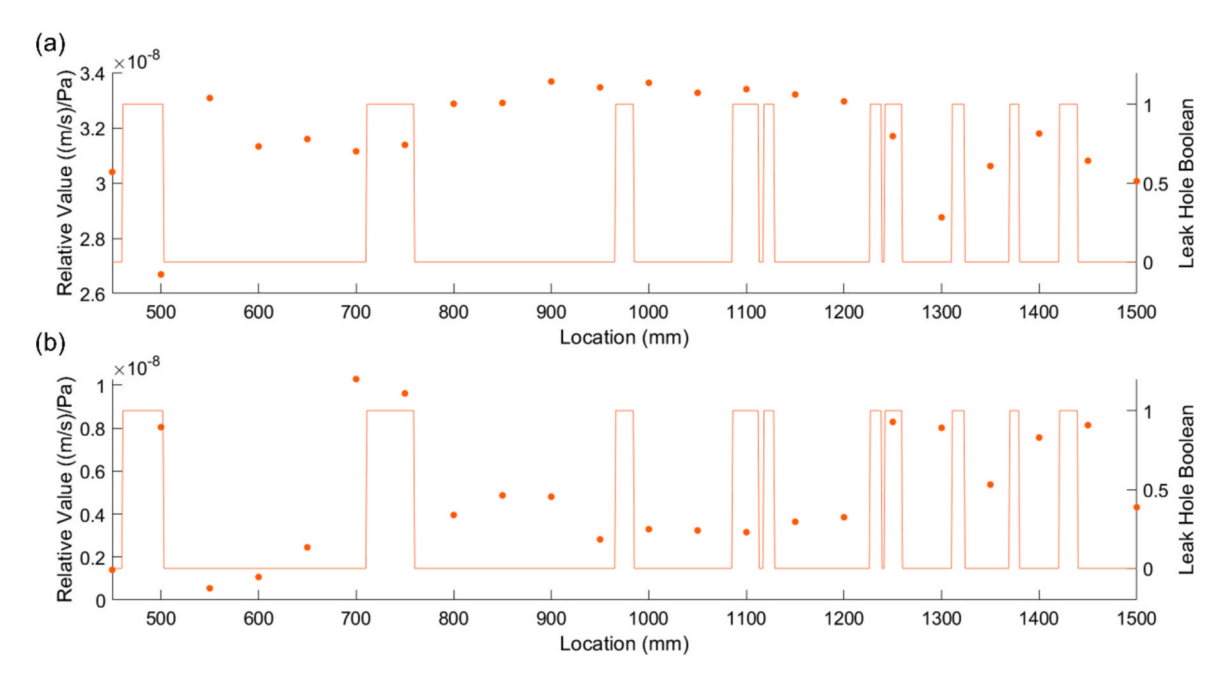


Fig. 16. A comparison of the ratio of the velocity to sound pressure amplitudes for: (a) *x*-velocity component; and (b) *y*-velocity component. The yellow line on each figure describes the position and size of the holes in the pipe.

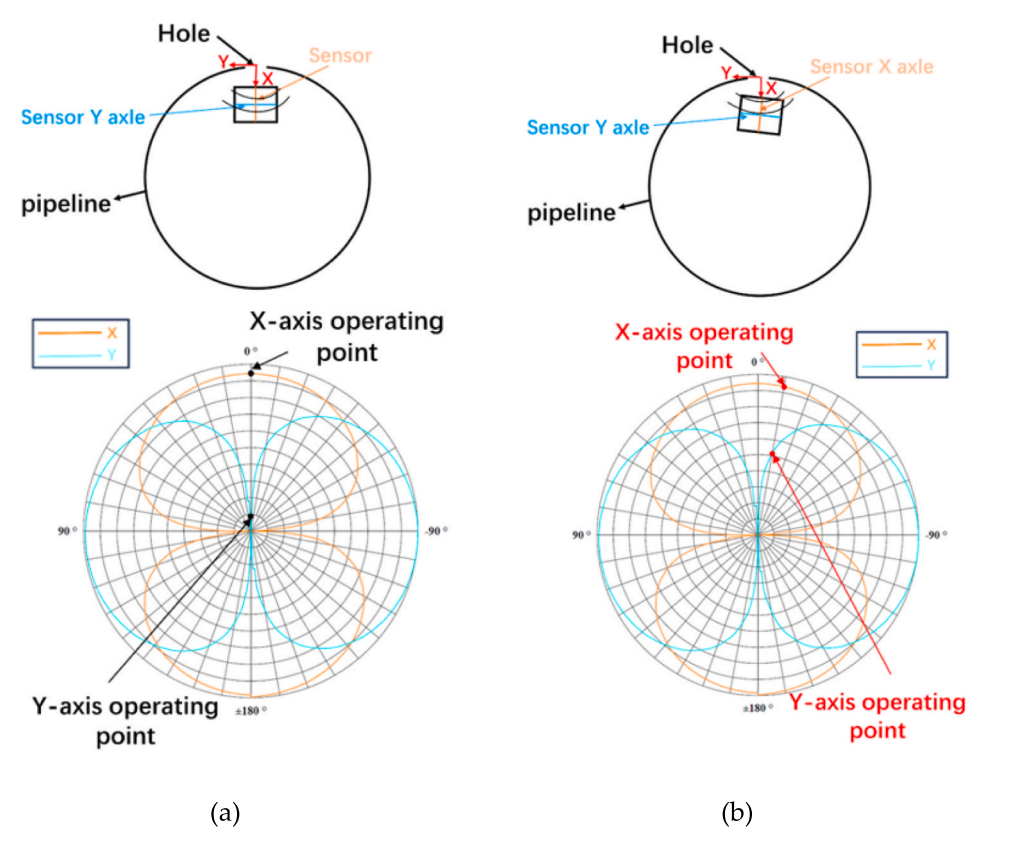


Fig. 17. An illustration of the effect of the hydrophone's directivity on its sensitivity in the *x*- and *y*-directions. (a) the cantilever arm is lined up perfectly along the *x*-axis; (b) the cantilever arm is misaligned with the *x*-axis at $\theta = 10^{\circ}$.

The Hilbert transform is a commonly used tool in signal processing, primarily employed for analyzing the phase and envelope of signals. After filtering, the signal underwent the Hilbert transformation to be represented as an analytic signal [28]:

$$Z(t) = V(t) + jH[V(t)]$$
(9)

The Hilbert envelope was then used to detect the magnitude of the analytic signal:

$$V_H(t) = \sqrt{V(t)^2 + (H[V(t)])^2}$$
 (10)

The process for extracting the signal's envelope is depicted in Fig. 14(b). Fig. 14 presents an example of the raw voltage signals received on the B&K and MEMS hydrophones at a distance of 600 mm Fig. 14(a) and their enveloped detected through the Hilbert transform (Fig. 14(b)). By calculating the average value of the Hilbert envelope, the average amplitude of the sensor output voltage can be computed. The variability in the amplitude of the signal emitted by the speaker was 10 %. Using the average amplitude and the sensitivity of the sensor, the velocities in each coordinate axis can be determined. At 65 Hz, the velocity along the x- and y-axes was measured by the vector hydrophone at various test points ranging from 450 mm to 1500 mm. The sensitivity of the vector hydrophone was calibrated to within 6 % [22]. The sound pressure values at each test point were measured by the B&K pressure hydrophone. The variation in the hydrophone sensitivity was estimated with B&K Type 4229 calibrator at 1 %. The average velocities along the xand y-axes, and sound pressure for each test point are shown in Fig. 15. The above variations in the sensitivity of the acoustic transducers used in the experiment provide a measure of uncertainty in the data presented in Figs. 15 and 16.

The results shown in Fig. 15 suggest that as the sensor approaches the speaker, the amplitude of the *x*-component of the velocity at various test points and sound pressure steadily increase. The behavior of the *x*-component of the acoustic velocity and sound pressure as a function of the distance is similar. This makes a good physical sense. The *x*-velocity component and the sound pressure do not exhibit aby significant changes as the sensor approaching a leakage hole. However, the amplitude of the *y*-component of the acoustic velocity at each test point shows a different trend compared to the *x*-component and the sound pressure. The amplitude of the *y*-velocity component exhibits fluctuations and an overall increasing trend mimicking the behavior of the sound pressure amplitude. In order to compensate for the distance effect the velocity amplitudes were normalized by the sound pressure. The results are shown in Fig. 16.

From the tests, we can observe that the presence of a leakage hole has a small effect on the *x*-velocity component. On the other hand, the *y*-velocity component shows a more noticeable dependence on the leakage hole locations. More significant variations up to an order of magnitude are observed in three particular segments: 460 mm-500 mm, 710 mm-760 mm, and 1220 mm-1440 mm (see Fig. 16). At these locations the *y*-velocity component measured near a leakage hole is significantly larger than that measured at a position without a leakage hole. In general, a relatively large amplitude of the normalized amplitude of the *y*-velocity component signifies the presence of a hole in the pipe's wall.

The behavior of the acoustic velocity vector measured in the experiment is complex and is not closely supported by the simulations reported in section 2.2. There are at least three reasons for this difference. Firstly, the length of the pipe used in the experiment is relatively short (2.5 m) in comparison with the wavelength (22.5 m at 65 Hz). This is likely to cause strong reflection and diffraction effects from the ends and rough edges of the exhumed pipe (see Fig. 9). These reflection and diffraction can distort and complicate the measured acoustic velocity field. Secondly, the pipe was placed in a container made of PCV panels and free surface close to the pipe walls. The PVC panels and free surface are likely to distort the sound field. Their effects were not accounted for in the COMSOL simulation. Finally, the presence of the vector hydrophone assembly (see Figs. 8 and 9) can distort the velocity field measured in the experiment. The diameter of the vector hydrophone protection case was 46 mm. It was larger than the size of the pipe leakage holes. Also, the small changes in the orientation of the vector hydrophone can affect the sensitivity of it in the x- and y-directions as illustrated in Fig. 17. These were difficult to control with the experimental setup.

5. Conclusions

This paper presents an application of MEMS vector hydrophones in the assessment of water supply pipeline conditions. Through theoretical analysis and numerical simulations, it was observed that the radial (xcomponent) and circumferential (y-component) particle velocities in the vicinity of the leakage holes exhibit complex characteristics at a low frequency. This behavior can potentially be used to identify the presence of a hole or wall thinning. The results from the experiment and data analysis revealed a linear relationship between the change in radial component of particle velocity amplitude near leakage holes and the acoustic pressure. The circumferential component of the particle velocity near some leakage holes exhibited a relatively high amplitude, up to an order of magnitude higher than that measured away from a leakage hole. This finding suggest that a leakage hole can be detected by measuring the circumferential component of particle velocity of the sound wave emitted at a relatively low frequency and with a very large wavelength. This is impossible to detect at such a frequency with a conventional pressure hydrophone.

There are some limitations in the conducted simulation and experiment. Ideally, the experiment should have been carried out on a pipe section surrounded by soil rather than being in a relatively small container made of PVC panels filled with 500 mm deep layer of water. The length of the pipe section should have been longer than the wavelength. Additionally, the orientation of the hydrophone's cantilever arm relative to the leakage hole could have affected the hydrophone's sensing capabilities, especially in perceiving the circumferential velocity component for the indication of the defects.

CRediT authorship contribution statement

Pengcheng Shi: Writing – review & editing, Writing – original draft, Visualization, Validation, Software, Methodology, Investigation, Formal analysis, Data curation, Conceptualization. Yicheng Yu: Writing – review & editing, Writing – original draft, Visualization, Validation, Supervision, Software, Methodology, Investigation, Formal analysis, Data curation, Conceptualization. Joanna Watts: Writing – review & editing, Writing – original draft, Visualization, Validation, Software, Methodology, Investigation, Formal analysis, Data curation, Conceptualization. Guojun Zhang: Writing – review & editing, Writing – original draft, Visualization, Supervision, Resources, Project administration, Methodology, Funding acquisition, Conceptualization. Kirill V. Horoshenkov: Writing – review & editing, Writing – original draft, Visualization, Validation, Supervision, Software, Resources, Project administration, Methodology, Investigation, Funding acquisition, Formal analysis, Data curation, Conceptualization.

Declaration of competing interest

The authors declare that they have no known competing financial interests or personal relationships that could have appeared to influence the work reported in this paper.

Acknowledgement

This work is supported by the UK Engineering and Physical Sciences Research Council (EPSRC) Programme Grant No. EP/S016813/1, National Natural Science Foundation of China (Grant No.52175553, 62274149).

Data availability

Data will be made available on request.

References

- Discover Water, treating sewage, 2020. Available at: https://discoverwater.co.uk/ treating-sewage (accessed 2020).
- [2] Yu Y, Worley R, Anderson S, et al. Microphone array analysis for simultaneous condition detection, localization, and classification in a pipe. J Acoust Soc Am 2023;153(1):367–83.
- [3] Taiwo R, Shaban IA, Zayed T. Development of sustainable water infrastructure: A proper understanding of water pipe failure. J Clean Prod 2023;398:136653. https://doi.org/10.1016/j.jclepro.2023.136653.
- [4] Yu Y, Horoshenkov KV, Tait S. Microphone array analysis of the first non-axisymmetric mode for the detection of pipe conditions. J Acoust Soc Am 2024;155 (1):575–87.
- [5] Liyanage KTH, Dhar AS. Effects of corrosion pits on wall stresses in cast-iron water mains. J Pipeline Syst Eng Pract 2017;8. https://doi.org/10.1061/(ASCE)PS.1949-1204.0000286.
- [6] Yu Y, Krynkin A, Li Z, et al. Analytical and empirical models for the acoustic dispersion relations in partially filled water pipes. Appl Acoust 2021;179:108076.
- [7] Ji J, Lai JH, Fu G, Zhang C, Kodikara J. Probabilistic failure investigation of small diameter cast iron pipelines for water distribution. Eng Fail Anal 2020;108: 104239. https://doi.org/10.1016/j.engfailanal.2019.104239.
- [8] Amaya-Gómez R, Sánchez-Silva M, Bastidas-Arteaga E, Schoefs F, Muñoz F. Reliability assessments of corroded pipelines based on internal pressure – A review. Eng Fail Anal 2019;98:190–214. https://doi.org/10.1016/j. engfailanal.2019.01.064.
- [9] Mazumder RK, Abdullahi MS, Li Y, Yu X. Reliability Analysis of Water Distribution Systems Using Physical Probabilistic Pipe Failure Method. J Water Resour Plan Manag 2019;145:04018097. https://doi.org/10.1061/(ASCE)WR.1943-5452.0001034.
- [10] Chen L, Duan Z, Li W, Yang G, Jia J, Ma L, et al. Physical Properties and Boundary Influence of Singularity in Fluid Pipelines Based on Vibration Wave's Transmission Characteristics. J Pipeline Syst Eng Pract 2022;13(1):04021066. https://doi.org/ 10.1061/(ASCFIPS.1049-1204.0000608
- [11] Dawood T, Elwakil E, Mayol Novoa H, Gárate Delgado JF. Watermain's failure index modeling via Monte Carlo simulation and fuzzy inference system. Eng Fail Anal 2022;134:106100. https://doi.org/10.1016/j.engfailanal.2022.106100.
- [12] Rainer A, Capell TF, Clay-Michael N, Demetriou M, Evans TS, Jesson DA, et al. What does NDE need to achieve for cast iron pipe networks? Infrastruct Asset Manag 2017;4(2):68–82.

- [13] Yu Y, Safari A, Niu X, Drinkwater B, Horoshenkov KV. Acoustic and ultrasonic techniques for defect detection and condition monitoring in water and sewerage pipes: A review. Appl Acoust 2021;183:108282.
- [14] Tang K, Parsons DJ, Jude S. Comparison of automatic and guided learning for Bayesian networks to analyse pipe failures in the water distribution system. Reliab Eng Syst Saf 2019;186:24–36. https://doi.org/10.1016/j.ress.2019.02.001.
- [15] Farh H, Ben Seghier MEA, Taiwo R, et al. Analysis and Ranking of Corrosion Causes for Water Pipelines: A Critical Review. npj Clean Water 2023;6(1):65.
- [16] Iwanek M, Suchorab P. Fractal Characteristics of Water Outflows on the Soil Surface after a Pipe Failure. Water 2024;16(9):1222.
- [17] Tchórzewska-Cieślak B, Pietrucha-Urbanik K, Piegdoń I. The Failure Risk Analysis of the Water Supply Network. Water 2023;15(21):3815.
- [18] Zhang B, Lei H, Hu X, et al. Time-Dependent Reliability of Corroded Mild Steel Pipes by Different Failure Modes. Int J Press Vessels Pip 2024;207:105100.
- [19] Wang R, Shen W, Zhang W, et al. Design and implementation of a jellyfish otolith-inspired MEMS vector hydrophone for low-frequency detection. Microsyst Nanoeng 2021;7:1. https://doi.org/10.1038/s41378-020-00227-w.
- [20] Wu Y, Zhang W, Wu D, et al. A directional algorithm from single MEMS vector hydrophone based on polynomial fitting and real-time attitude compensation. Measurement 2024;227:114195. https://doi.org/10.1016/j. measurement.2024.114195.
- [21] Xue C, Chen S, Zhang W, Zhang B, Zhang G, Qiao H. Design, fabrication, and preliminary characterization of a novel MEMS bionic vector hydrophone. Microelectron J 2007;38:1021–6.
- [22] Geng Y, Ren W, Zhang G, Chen P, Zhu S, Zhang Y, et al. Design and Fabrication of Hollow Mushroom-Like Cilia MEMS Vector Hydrophone. IEEE Trans Instrum Meas 2023;72:1–8.
- [23] Morse PM, Ingard KU. Theoretical Acoustics. Princeton, NJ, USA: Princeton University Press; 1986.
- [24] Fuller CR, Fahy FJ. Characteristics of wave propagation and energy distributions in cylindrical elastic shells filled with fluid. J Sound Vib 1982;81:501–18.
- [25] Muggleton JM. Yan J, Wavenumber prediction and measurement of axisymmetric waves in buried fluid-filled pipes: Inclusion of shear coupling at a lubricated pipe/ soil interface. J Sound Vib 2013;332:1216–30.
- [26] Rienstra SW, Tester BJ. An analytic Green's function for a lined circular duct containing uniform mean flow. J Sound Vib 2008;317:994–1016.
- [27] Meng L, Lan J. Principles and Applications of Sensors. 3rd ed. Beijing, China: Electronic Industry Press; 2015.
- [28] Blackledge J. Digital Signal Processing. 2nd ed. Dublin, Ireland: Technological University Dublin; 2006.